Thermal control of graphene morphology: A signature of its intrinsic surface tension

R. Ramírez* and C. P. Herrero

Instituto de Ciencia de Materiales de Madrid (ICMM), Consejo Superior de Investigaciones Científicas (CSIC), Campus de Cantoblanco, 28049 Madrid, Spain

(Received 16 March 2018; revised manuscript received 27 April 2018; published 18 June 2018)

The surface tension σ of free-standing graphene is studied by path-integral simulations as a function of the temperature and the in-plane stress. Even if the applied stress vanishes, the membrane displays a finite surface tension σ due to the coupling between the bending oscillations and the real area of the membrane. Zero-point effects for σ are significant below 100 K. Thermal cooling drives the membrane from a planar to a wrinkled morphology. Upon heating the change is reversible and shows hysteresis, in agreement with recent experiments performed on supported graphene.

DOI: 10.1103/PhysRevB.97.235426

I. INTRODUCTION

Graphene, in contrast to the complex lipid bilayer membranes, is an ideal system to understand physical effects of a two-dimensional (2D) layer fluctuating in 3D space [1,2]. Several experiments have shown that the morphology of graphene can be reversibly changed from a wrinkled configuration at low temperature to a planar one at high temperature, typically in a range of 100–600 K [3–9]. This change has been qualitatively explained by the presence of an underlying substrate. The mismatch between the expansion coefficients of the substrate and graphene should produce mechanical stresses that drive the morphology change. Wrinkles found in the experiments were periodic and static, with amplitudes several orders of magnitude larger than those arising from thermal fluctuations [3]. Such a planar-to-wrinkled transition may, however, be a pure thermal effect and equally appear in free-standing graphene, in the absence of any substrate. In fact, for graphene under a small compressive stress, the planar symmetry is broken, so that wrinkles appear to stabilize the system at relatively low temperatures [10,11]. Rising the temperature introduces thermal fluctuations in the system that can help to reduce the effective stress suffered by the graphene layer and thus to recover the planar phase. This uncommon behavior is investigated here by atomistic simulations.

II. SIMULATION METHOD

Quantum path-integral and classical simulations of graphene, performed with an in-house code, are presented as a function of temperature (T) and in-plane stress (τ). Our goal is to show that, under a *constant* applied stress τ, a planar free-standing layer wrinkles by lowering the temperature. Wrinkling is a direct consequence of a mechanical instability in the bending of the planar layer [12]. In the thermodynamic limit, this instability (spinodal point) [13] corresponds to a vanishing surface tension ($\sigma \equiv 0$) of the layer. Our analysis will provide insight into the dependence of the surface tension σ of graphene with the applied stress τ and the temperature.

The implementation of path-integral (PI) molecular dynamic (MD) simulations is based on an isomorphism between the quantum system and a fictitious classical one, in which the quantum particle (here a C nucleus) is described by a ring polymer composed of N_{Tr} (Trotter number) beads [14–18]. This becomes exact in the limit $N_{Tr} \to \infty$. N_{Tr} was taken here proportional to the inverse temperature, $N_{Tr}T = 6000$ K, a condition that makes the numerical error of solving the path integral nearly temperature independent. The classical limit is achieved just by setting $N_{Tr} = 1$. The empirical interatomic LCBOPII model was employed for the calculation of interatomic forces and potential energy [19]. This empirical potential has been used in the past to study the elastic behavior and the out-of-plane crumpling of graphene [20–22]. The phonon dispersion curves of graphene and graphite in the harmonic limit, as derived from the diagonalization of the dynamical matrix with the LCBOPII model were presented in Fig. 1 of Ref. [23]. The phonon dispersion of graphite displays a reasonable overall agreement with experimental data, considering that the potential was not specifically fitted to reproduce the force constants of graphite [23]. The largest disagreement was found for the bending rigidity κ, that amounts to 0.7 eV in the harmonic zero-temperature limit, while the best fit to available theoretical and experimental data reported by Lambin amounts to 1.6 eV [11]. According to previous simulations [24–28], the original LCBOPII parametrization has been slightly modified to increase the zero-temperature bending constant of graphene to 1.5 eV [29]. For the improved potential, the phonon dispersion curves of graphene remain unchanged for the in-plane modes [23], while the improved optical (ZO) and acoustic (ZA) out-of-plane modes were presented in Fig. 1(b) of Ref. [24]. We have also compared the improved ZA and ZO harmonic dispersion curves of the LCBOPII model with those corresponding to a density-functional-based tight-binding (TB) model [30], that has been previously employed to study the out-of-plane wrinkling of graphene [31]. We find that the long wavelength limit of the ZA branch is nearly identical for both methods.

*ramirez@icmm.csic.es

The simulations have been performed in the $N\tau T$ ensemble. The simulation cell contains N carbon atoms and 2D periodic boundary conditions were applied with translation vectors defining the (x,y) plane. The area of the 2D simulation cell is NA_p. The in-plane stress τ is the lateral force per unit length at the boundary of the simulation cell [32]. It is defined as one half of the trace of the in-plane stress tensor $(\tau_{xx}+\tau_{yy})/2$. The estimator employed for τ_{xx} and τ_{yy} can be found in Refs. [24] and [27] for classical and quantum cases, respectively. Cells sizes with 960 atoms were studies, and typical $N\tau T$ simulations consisted on 10^6 MD steps for equilibration and 8×10^6 steps for the calculation of ensemble average quantities. The analysis of the simulation trajectories was performed in subsets of 16 000 different configurations, stored at equidistant times along the simulation run. Error bars were derived by averaging results obtained from at least two independent full trajectories. The time step of the simulations was 1 fs. Further technical details are identical to those already published in our previous studies of graphene [24–28].

III. LAYER MORPHOLOGY

An example of the different morphologies found for graphene is given in Fig. 1. These configurations were obtained by path-integral simulations under isotropic compressive in-plane stress ($\tau = 0.025$ eV/Å^2), but at different temperatures of 100 and 300 K, respectively. The wrinkled and planar morphologies of graphene display different values of the projected in-plane area NA_p, while the real surface areas NA are similar (see Fig. 1). The real surface area per atom A is larger than A_p, if the layer is not strictly flat. This area NA was calculated by triangulation, with six contiguous triangles filling each hexagon of the layer. They share a common vertex located at the barycenter of the hexagon and each triangle has a CC bond as a side. An ongoing discussion in biological membranes is that their thermodynamic properties should be described using the notion of a real surface A rather than an in-plane projection A_p [33]. The contrast between the extensive variables, NA_p and NA [34,35], can be translated to their conjugate intensive ones, namely the in-plane stress τ and the negative of the surface tension $-\sigma$, respectively [32,36,37]. In the following, we will show that the increase of the surface tension σ with raising temperature drives the change from the wrinkled to the planar morphology. This effect is a counterintuitive property of the solid membrane. Liquid surfaces, say water, behave in the opposite way, their surface tension σ decreases as temperature increases [38].

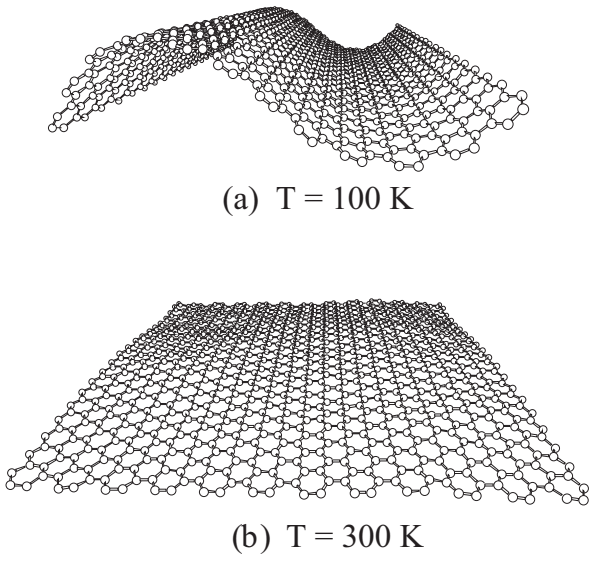

FIG. 1. Morphology of free-standing graphene derived from PIMD $N\tau T$ simulations at the uniform compressive in-plane stress $\tau = 0.025$ eV/Å^2. The equilibrium configuration is wrinkled at 100 K (a) but planar at 300 K (b). Wrinkles are more easily formed along the armchair direction.

IV. SURFACE TENSION

The calculation of the surface tension σ has been performed by two routes. The first one is based on the Fourier analysis of the amplitude of the out-of-plane atomic fluctuations in the planar morphology,

$$H(\mathbf{k}) = \frac{1}{N}\sum_{j=1}^{N} h_j e^{-i\mathbf{k}\mathbf{u}_j}. \tag{1}$$

$\mathbf{k}$ is a 2D reciprocal vector commensurate with the employed simulation cell. In the case of a classical MD simulation $\mathbf{r}_j = (\mathbf{u}_j, h_j)$ are the atomic positions, with $\mathbf{u}_j$ a 2D vector in the (x,y) plane and h_j the height of the atom with respect to the mean layer plane. In the case of a quantum simulation $\mathbf{r}_j$ are centroid coordinates, which represent the center of mass of the cyclic paths associated with a given nucleus [39]. The estimation of $H(\mathbf{k})$ using centroid coordinates, instead of bead coordinates, is justified because the centroid density represents the static response of the quantum system to the application of an external force [40]. Thus, the mean-square amplitude $\bar{H}^2 = HH^*$ can be related to the dispersion relation, $\rho\omega^2$, of the acoustic ZA modes as

$$\langle \bar{H}(\mathbf{k})^2 \rangle = \frac{k_B T}{A_p \rho [\omega(\mathbf{k})]^2}, \tag{2}$$

where the angle brackets indicate an average over the whole trajectory, k_B is the Boltzmann constant, and ρ is the density of the layer. This relation between spatial centroid fluctuations $\langle \bar{H}^2 \rangle$, and vibrational wave numbers ω has been applied in PI simulations to study anharmonic shifts in the vibrational frequencies of solids and molecules [41–43]. The long-wavelength limit of the ZA modes is well described by the dispersion relation

$$\rho[\omega(k)]^2 = \sigma k^2 + \kappa k^4, \tag{3}$$

where σ is the surface tension, κ the bending constant of the layer, and $k = |\mathbf{k}|$. Numerical details of the fit of the simulated amplitudes $\langle \bar{H}^2 \rangle$ to the dispersion relation $\rho\omega^2$, to obtain the parameters σ and κ, are given in Ref. [24]. In particular, Fig. 1(b) of this reference shows that this numerical approach accurately reproduces, in the classical low temperature limit, the analytical dispersion curve of the ZA modes derived by diagonalization of the vibrational dynamical matrix of the employed potential. The dispersion relation in Eq. (3) assumes

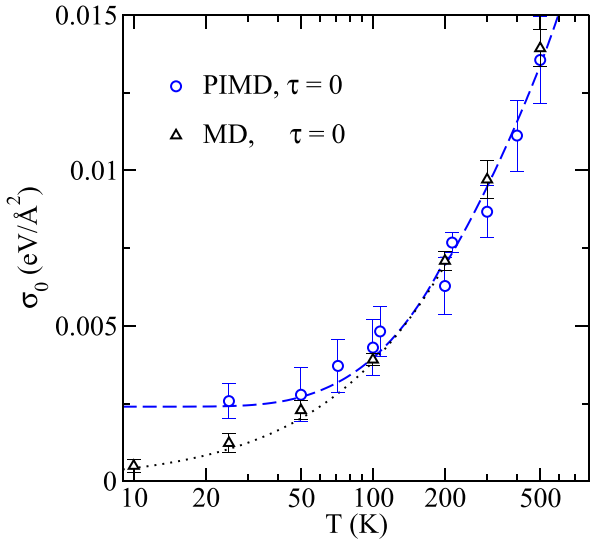

FIG. 2. Surface tension of free-standing graphene as a function of temperature. Results derived from $N\tau T$ simulations with isotropic cell fluctuations at in-plane stress $\tau = 0$. Quantum results are shown as open circles. Classical results are displayed by open triangles. Lines are guides to the eye.

spatial isotropy in the 2D $\mathbf{k}$ space, being accurate for $k \lesssim 0.5$ Å^{-1} [24].

The surface tension, $\sigma_0 \equiv \sigma(\tau = 0)$, in the quantum and classical cases has been derived from $N\tau T$ simulations with isotropic cell fluctuations and vanishing in-plane stress ($\tau = 0$) as a function of temperature. The results for $N = 960$ atoms are presented in Fig. 2. The classical limit of σ_0 is somewhat larger than that presented in Ref. [24]. The latter was derived with full (i.e., nonisotropic) cell fluctuations [44], allowing for an additional relaxation of the surface tension. Finite size errors in σ_0 are small for the employed simulation cell [24]. The surface tension vanishes in the classical $T \to 0$ limit as the absence of bending implies that $A \equiv A_p$ and $-\sigma \equiv \tau$. According to Eq. (3) the value $\sigma = 0$ represents the limit for the mechanical stability of a flat layer. For $\sigma < 0$, the long-wavelength ZA modes ($k \to 0$) become mechanically unstable, as there appear imaginary wave numbers in $\omega(k)$ [10,45]. The classical surface tension σ increases with temperature, implying that the planar morphology is stabilized [46], as the dispersion relation moves away from the mechanical instability at $\sigma = 0$.

Quantum effects in σ_0 are significant at temperatures below 100 K. Zero-point vibrations imply a small but finite bending of the layer in the $T \to 0$ limit. The extrapolation indicates a finite surface tension of $\sigma_0 \sim 2.5$ meV/Å^2 as $T \to 0$. This positive value of σ_0 implies that quantum zero-point vibrations stabilize the planar morphology of the layer with respect to the classical limit.

Our nonperturbational results for σ_0 are in good agreement with recent analytical work based on a perturbational treatment of anharmonicity in a continuous model of the solid membrane [47–50], although this term is absent in other perturbation theory treatment [51]. A surface tension σ implies a finite acoustic sound velocity $v = (\sigma/\rho)^{1/2}$ for the out-of-plane modes. The surface tension at 300 K is $\sigma_0 = 8.7 \pm 0.8$ meV/Å^2, that translates into an acoustic sound velocity of 0.4 km/s.

In contrast to our MD results for σ_0, previous Monte Carlo (MC) works claim that such a term should not be present [20,52]. Both MD and MC methods should provide identical results. The origin of this disagreement is not clear, but it might be due to inaccuracies in the sampling of the sluggish long-wavelength modes. Several general considerations on the appearance of a finite surface tension in an unstressed layer are appropriate. The difference between the real and projected areas of a flat layer, A and A_p, has been demonstrated experimentally by their different stress-strain curves [35], elastic constants [25,53], and thermal expansion coefficients [34]. It seems physically reasonable that when the extensive variables (NA_p, NA) are different, their conjugate intensive ones, $(\tau, -\sigma)$, might be also different. Time reversal symmetry in the dynamical vibrational matrix implies that the ZA phonon dispersion satisfies $\omega^2(\mathbf{k}) = \omega^2(-\mathbf{k})$. Equation (3) represents the first terms of the Maclaurin series of an analytical even phonon dispersion with coefficients depending on (τ, T). The simulations in Refs. [20,52] were fitted to a model following a nonanalytical dispersion relation, $\omega^2(\mathbf{k}) \propto k^{4-\eta}$, with the anomalous exponent $\eta \sim 0.82$. The theoretical basis of this model is the self-consistent screening approximation (SCSA) applied to an unstressed membrane. This model also predicts a negative Poisson ratio ν [54]. However experimental data [55] and computer simulations [21] show that $\nu \sim 0.16$ for graphene. A finite term σ_0 is believed to be prohibited for a continuous unstressed membrane, since it violates the rotation invariance [56]. However, in a more realistic atomistic description of a membrane a finite σ_0 is possible without loss of rotational invariance [57].

The consideration that σ is the thermodynamic variable conjugate to the real area, NA, suggests a second route to calculate σ from computer simulations [33,58]. The average value of the area A as a function of τ is presented in Fig. 3(a) at 300 K. The real area A in the planar morphology decreases when the in-plane stress increases from tensile ($\tau < 0$) to compressive ($\tau > 0$) ones. We have checked that the stress-strain curve derived from Fig. 2(a) is in good agreement with those derived from Raman spectroscopy in Refs. [35,59]. The planar morphology becomes unstable for the in-plane stress displayed by a vertical broken line in Fig. 3(a). The change in morphology affects the area A, and one observes that the slope of $A(\tau)$ changes its sign when the layer wrinkles. The 2D modulus of hydrostatic compression B [60] is the inverse of the compressibility of the real area A. It has been derived from the fluctuation formula [25]

$$B = \frac{k_B T \langle A \rangle}{N(\langle A^2 \rangle - \langle A \rangle)^2}, \tag{4}$$

and is displayed as a function of τ in Fig. 3(b). The results for $A(\tau)$ and $B(\tau)$ can be combined to obtain the surface tension σ by numerical integration of the formal relation between the compressional modulus and the Hooke's law of elasticity [33,58]:

$$\frac{d\sigma}{dA} = \frac{B}{A}. \tag{5}$$

As integration constant we used the value $\sigma_0 = 8.7$ meV/Å^2 at $\tau = 0$ (see Fig. 2). By combining the integrated function $\sigma(A)$ and $A(\tau)$, one gets the function $\sigma(\tau)$ in Fig. 3(c) (solid

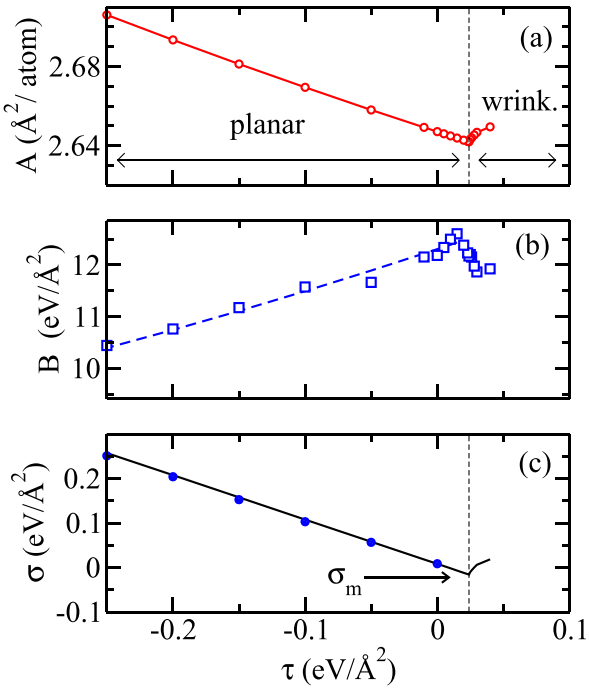

FIG. 3. (a) Dependence of the real area A of graphene with the in-plane stress τ as derived from PIMD simulations at 300 K. The solid line is a guide to the eye. The vertical dashed line indicates the transition from a planar to a wrinkled morphology of the layer. (b) The corresponding 2D compressional modulus B as derived from the fluctuations of the real area A. The broken line is a guide to the eye. (c) The full line displays the surface tension σ obtained from the numerical integration of B/A according to Eq. (5). The full circles are obtained from the analysis of the ZA amplitudes by Eqs. (2) and (3). The surface tension σ is minimum ($\sigma_m = -24$ meV/Å^2) when the layer changes its morphology.

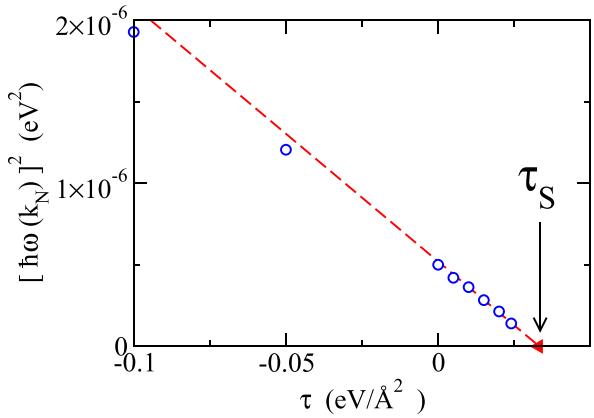

FIG. 4. Square of the energy quantum of the ZA mode with lowest energy $\omega(k_N)$ from PIMD simulations with $N = 960$ atoms. The open circles were derived at 300 K as a function of the in-plane stress τ. The broken line is a linear fit to the simulation data with $\tau \geqslant 10$ meV/Å^2. $\omega(k_N)$ vanishes at the in-plane spinodal stress, $\tau_S = 33$ meV/Å^2 (full triangle).

line). The surface tension attains its minimum value (σ_m) when the layer becomes wrinkled. Note the similar behavior of the conjugate variables, σ and A, with the in-plane stress τ in Figs. 3(a) and 3(c). An independent derivation of σ from the Fourier analysis of the ZA fluctuations is shown as full symbols for several values of τ in Fig. 3(c). The agreement between both methods is excellent. For the planar morphology at a constant temperature, the surface tension and the in-plane stress are related as $\sigma = \sigma_0 - \tau$ [25]. This relation is not valid for the wrinkled morphology as the slope of the function $\sigma(\tau)$ becomes positive. Compressive stresses slightly larger than those in Fig. 3 produce a collapse of the graphene structure.

The wrinkled morphology of the layer is a consequence of an instability of the long-wavelength ZA modes [12], whose dispersion relation is given by Eq. (3). The energy quantum of the ZA mode with lowest energy, $\omega(k_N)$, of a planar layer is plotted in Fig. 4 as a function of the in-plane stress. $k_N = 2\pi/(NA_p)^{1/2}$ is the modulus of the $\mathbf{k}$ vector closest to the origin. A mechanical instability appears when $\omega(k_N) \to 0$ [10,45]. With the employed simulation cell, this condition is met at the spinodal in-plane stress $\tau_S = 33$ meV/Å^2, as derived from the extrapolation in Fig. 4. According to Eqs. (3), the spinodal in-plane stress (τ_S) and the spinodal surface tension (σ_S) are related as

$$\sigma_S \equiv \sigma_0 - \tau_S = -\kappa k_N^2 . \quad (6)$$

Note that the r.h.s of this equation is a finite size contribution. In the thermodynamic limit, $N \to \infty$, then $k_N \to 0$, and the spinodal in-plane stress becomes $\tau_S = \sigma_0$. For finite size systems the planar morphology is comparatively more stable, as if $k_N > 0$ then the spinodal surface tension will be $\sigma_S < 0$. For the employed simulation cell ($N = 960$), the values of κ and k_N derived from the PIMD trajectory at 300 K and $\tau = 0$ are $\kappa = 1.6$ eV, and $k_N = 0.123$ Å^{-1}, respectively. Considering the value of τ_S from Fig. 4, one derives from Eq. (6) that $\sigma_0 = 9$ meV/Å^2. This new estimation of σ_0 at 300 K agrees closely with the value shown in Fig. 2.

V. TEMPERATURE CYCLE

Our simulations can be compared to recent experimental data that demonstrate the thermal control of the graphene morphology [3–9]. To this aim we have performed nonequilibrium simulations at constant in-plane stress τ with temperature varying at a uniform rate of 20 K/ns in cycles between 1000 and 25 K. A cycle consists of 10^8 MD steps. The simulations are performed in the classical limit, as quantum effects in the morphology of the layer are significant only below 100 K. The morphology has been monitored by the value of the projected area, A_p, along the thermal cycle. The results for three different in-plane compressive stresses are displayed in Fig. 5. An arrow pointing down (up) indicates that the temperature is decreasing (increasing). At high temperature the in-plane area has a value of $A_p \sim 2.6$ Å^2/atom, typical of a planar morphology. At the scale of the figure, the area A_p remains nearly constant as the temperature decreases. We observe that by cooling the flat layer becomes wrinkled and the projected area A_p jumps to a value <2 Å^2/atom. The lower the compressive in-plane stress τ, the lower the temperature of the wrinkling transition. By cooling down to 25 K the projected area of the wrinkled morphology decreases monotonically, showing

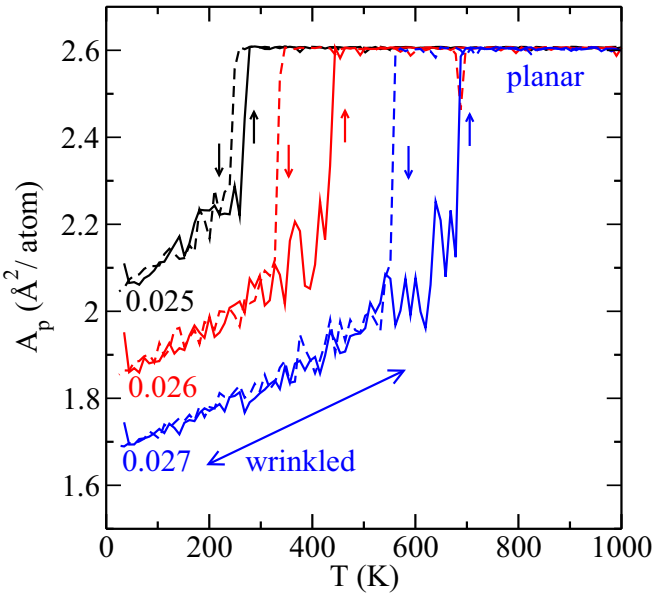

FIG. 5. Dependence of the projected area of graphene with temperature in a thermal cycle between 1000 and 25 K from classical $N\tau T$ simulations. Results for three different isotropic in-plane compressive stresses (τ, in eV/Å^2). Small arrows up (down) indicate the heating (cooling) process of the cycle.

that the lower the temperature the larger the amplitude of the surface wrinkles of a free-standing layer [61]. The area A_p in the wrinkled morphology is extremely sensitive to the applied in-plane stress. Therefore, the strain in the variable A_p for the wrinkled morphology should be strongly dependent on external conditions, such as the substrate and the size of the sample. A comparison to experimental data for this variable is only sensible in a qualitative level. From an experimental point of view, there appears an ample range of periodic wrinkling morphologies, from amplitudes of 1 Å and wavelengths of 8 Å [31], to amplitudes of 300 Å and wavelengths of 25 μm [3]. In the reverse cycle, upon heating from 25 K up to 1000 K, one observes that the change in morphology is reversible and there appears hysteresis in the transition temperature.

VI. SUMMARY

Summarizing, the surface tension σ of graphene, as the variable conjugate to the real surface area A has been determined by three different methods: by analysis of the Fourier transform of the bending fluctuations, by integration of the 2D compressional modulus associated to the real area A, and by derivation of the spinodal in-plane stress (τ_S) in a finite size sample. The mutual agreement reveals that our analysis is thermodynamically sound, providing insight into this intrinsic property. The consideration that the bending of a planar layer increases its surface tension allows us to rationalize that quantum zero-point effects as well as a rise of temperature increase the stability of a planar morphology. Quantum effects in the surface tension are significant below 100 K.

Our simulations provide insight into experiments showing a thermal control of the graphene morphology [3–9]. The temperature changes the bending of the layer while the latter modifies the surface tension. The higher the temperature, the larger the surface tension, favoring a planar layer. The decrease of the surface tension with lowering temperature produces wrinkles when the planar layer approaches its stability limit (spinodal point). This transition is reversible and shows hysteresis in agreement to experiments performed on supported graphene [3–9]. The mechanical instability in the bending of the planar layer displays a size effect. The cutoff of the long-wavelength bending modes in a finite size layer implies an increased stability of its planar morphology. In the thermodynamic limit $N \to \infty$, the spinodal point of a planar layer corresponds to a vanishing surface tension. The expectation that a membrane in thermal equilibrium has vanishing surface tension, because its free energy should be minimal with respect to the area of the membrane, is not met for crystalline graphene. This is a consequence of the coupling between the real surface area and the bending of the layer.

ACKNOWLEDGMENTS

This work was supported by Dirección General de Investigación, MINECO (Spain) through Grant No. FIS2015-64222-C2-1-P. We thank the support of J. H. Los in the implementation of the LCBOPII potential.

[1] R. Roldan, L. Chirolli, E. Prada, J. Angel Silva-Guillen, P. San-Jose, and F. Guinea, Chem. Soc. Rev. **46**, 4387 (2017).
[2] B. Amorim, A. Cortijo, F. de Juan, A. Grushin, F. Guinea, A. Gutiérrez-Rubio, H. Ochoa, V. Parente, R. Roldán, P. San-Jose, J. Schiefele, M. Sturla, and M. Vozmediano, Phys. Rep. **617**, 1 (2016).
[3] W. Bao, F. Miao, Z. Chen, H. Zhang, W. Jang, C. Dames, and C. N. Lau, Nat. Nanotechnol. **4**, 562 (2009).
[4] H. Hattab, A. T. N'Diaye, D. Wall, C. Klein, G. Jnawali, J. Coraux, C. Busse, R. van Gastel, B. Poelsema, T. Michely, F.-J. Meyer zu Heringdorf, and M. Horn-von Hoegen, Nano Lett. **12**, 678 (2012).
[5] W. Bao, K. Myhro, Z. Zhao, Z. Chen, W. Jang, L. Jing, F. Miao, H. Zhang, C. Dames, and C. N. Lau, Nano Lett. **12**, 5470 (2012).
[6] Y. Zhang, Q. Fu, Y. Cui, R. Mu, L. Jin, and X. Bao, Phys. Chem. Chem. Phys. **15**, 19042 (2013).
[7] K.-K. Bai, Y. Zhou, H. Zheng, L. Meng, H. Peng, Z. Liu, J.-C. Nie, and L. He, Phys. Rev. Lett. **113**, 086102 (2014).
[8] S. Deng and V. Berry, Materials Today **19**, 197 (2016).
[9] L. Meng, Y. Su, D. Geng, G. Yu, Y. Liu, R.-F. Dou, J.-C. Nie, and L. He, Appl. Phys. Lett. **103**, 251610 (2013).
[10] P. L. de Andres, F. Guinea, and M. I. Katsnelson, Phys. Rev. B **86**, 245409 (2012).
[11] P. Lambin, Appl. Sci. **4**, 282 (2014).
[12] J. Rodríguez-Hernández, Prog. Polym. Sci. **42**, 1 (2015).
[13] H. J. Maris, Phys. Rev. Lett. **66**, 45 (1991).
[14] R. P. Feynman, *Statistical Mechanics* (Addison-Wesley, New York, 1972).

[15] D. M. Ceperley, Rev. Mod. Phys. **67**, 279 (1995).
[16] M. E. Tuckerman, in *Quantum Simulations of Complex Many–Body Systems: From Theory to Algorithms*, edited by J. Grotendorst, D. Marx, and A. Muramatsu (NIC, FZ Jülich, 2002), p. 269.
[17] C. P. Herrero and R. Ramírez, J. Phys.: Condens. Matter **26**, 233201 (2014).
[18] C. Cazorla and J. Boronat, Rev. Mod. Phys. **89**, 035003 (2017).
[19] J. H. Los, L. M. Ghiringhelli, E. J. Meijer, and A. Fasolino, Phys. Rev. B **72**, 214102 (2005).
[20] A. Fasolino, J. H. Los, and M. I. Katsnelson, Nat. Mater. **6**, 858 (2007).
[21] J. H. Los, A. Fasolino, and M. I. Katsnelson, Phys. Rev. Lett. **116**, 015901 (2016).
[22] J. H. Los, M. I. Katsnelson, O. V. Yazyev, K. V. Zakharchenko, and A. Fasolino, Phys. Rev. B **80**, 121405 (2009).
[23] L. Karssemeijer and A. Fasolino, Surf. Sci. **605**, 1611 (2011).
[24] R. Ramírez, E. Chacón, and C. P. Herrero, Phys. Rev. B **93**, 235419 (2016).
[25] R. Ramírez and C. P. Herrero, Phys. Rev. B **95**, 045423 (2017).
[26] C. P. Herrero and R. Ramírez, J. Chem. Phys. **145**, 224701 (2016).
[27] C. P. Herrero and R. Ramírez, Phys. Chem. Chem. Phys. **19**, 31898 (2017).
[28] C. P. Herrero and R. Ramírez, J. Chem. Phys. **148**, 102302 (2018).
[29] J. H. Los (private communication).
[30] D. Porezag, T. Frauenheim, T. Köhler, G. Seifert, and R. Kaschner, Phys. Rev. B **51**, 12947 (1995).
[31] L. Tapasztó, T. Dumitrič, S. J. Kim, P. Nemes-Incze, C. Hwang, and L. P. Biró, Nat. Phys. **8**, 739 (2012).
[32] J.-B. Fournier and C. Barbetta, Phys. Rev. Lett. **100**, 078103 (2008).
[33] E. Chacón, P. Tarazona, and F. Bresme, J. Chem. Phys. **143**, 034706 (2015).
[34] M. Pozzo, D. Alfè, P. Lacovig, P. Hofmann, S. Lizzit, and A. Baraldi, Phys. Rev. Lett. **106**, 135501 (2011).
[35] R. J. T. Nicholl, N. V. Lavrik, I. Vlassiouk, B. R. Srijanto, and K. I. Bolotin, Phys. Rev. Lett. **118**, 266101 (2017).
[36] P. Tarazona, E. Chacón, and F. Bresme, J. Chem. Phys. **139**, 094902 (2013).
[37] S. A. Safran, *Statistical Thermodynamics of Surfaces, Interfaces, and Membranes* (Addison-Wesley, Reading, Massachusetts, 1994).
[38] W. V. Kayser, J. Colloid Interface Sci. **56**, 622 (1976).
[39] R. Ramírez and T. López-Ciudad, in *Quantum Simulations of Complex Many–Body Systems: From Theory to Algorithms*, edited by J. Grotendorst, D. Marx, and A. Muramatsu (NIC, FZ Jülich, 2002), p. 325.
[40] R. Ramírez and T. López-Ciudad, Phys. Rev. Lett. **83**, 4456 (1999).
[41] R. Ramírez and T. López-Ciudad, J. Chem. Phys. **115**, 103 (2001).
[42] R. Ramírez and C. P. Herrero, Phys. Rev. B **72**, 024303 (2005).
[43] C. P. Herrero and R. Ramírez, Phys. Rev. B **82**, 174117 (2010).
[44] G. J. Martyna, D. J. Tobias, and M. L. Klein, J. Chem. Phys. **101**, 4177 (1994).
[45] F. Ma, H. B. Zheng, Y. J. Sun, D. Yang, K. W. Xu, and P. K. Chu, Appl. Phys. Lett. **101**, 111904 (2012).
[46] J. C. Meyer, A. K. Geim, M. I. Katsnelson, K. S. Novoselov, T. J. Booth, and S. Roth, Nature (London) **446**, 60 (2007).
[47] V. Adamyan, V. Bondarev, and V. Zavalniuk, Phys. Lett. A **380**, 3732 (2016).
[48] V. N. Bondarev, V. M. Adamyan, and V. V. Zavalniuk, Phys. Rev. B **97**, 035426 (2018).
[49] B. Amorim, R. Roldán, E. Cappelluti, A. Fasolino, F. Guinea, and M. I. Katsnelson, Phys. Rev. B **89**, 224307 (2014).
[50] K. H. Michel, S. Costamagna, and F. M. Peeters, physica status solidi (b) **252**, 2433 (2015).
[51] I. S. Burmistrov, I. V. Gornyi, V. Y. Kachorovskii, M. I. Katsnelson, and A. D. Mirlin, Phys. Rev. B **94**, 195430 (2016).
[52] J. Hašík, E. Tosatti, and R. Martoňák, Phys. Rev. B **97**, 140301 (2018).
[53] R. J. T. Nicholl, H. J. Conley, N. V. Lavrik, I. Vlassiouk, Y. S. Puzyrev, V. P. Sreenivas, S. T. Pantelides, and K. I. Bolotin, Nat. Commun. **6**, 8789 (2015).
[54] P. L. Doussal and L. Radzihovsky, Ann. Phys. **392**, 340 (2018).
[55] A. Politano, A. R. Marino, D. Campi, D. Farías, R. Miranda, and G. Chiarello, Carbon **50**, 4903 (2012).
[56] J.-W. Jiang, B.-S. Wang, J.-S. Wang, and H. S. Park, J. Phys.: Condens. Matter **27**, 083001 (2015).
[57] S. Kumar, K. P. S. S. Hembram, and U. V. Waghmare, Phys. Rev. B **82**, 115411 (2010).
[58] Q. Waheed and O. Edholm, Biophys. J. **97**, 2754 (2009).
[59] R. Ramírez and C. P. Herrero (unpublished).
[60] F. Behroozi, Langmuir **12**, 2289 (1996).
[61] D. A. Kirilenko, A. T. Dideykin, and G. Van Tendeloo, Phys. Rev. B **84**, 235417 (2011).